Available online at www.sciencedirect.com
ScienceDirect
International Journal of Heat and Fluid Flow 29 (2008) 527–539
International Journal of HEAT AND FLUID FLOW
www.elsevier.com/locate/ijhff

Computational study of buoyancy effects in a laminar starting jet

Rajani P. Satti [a,1], Ajay K. Agrawal [b,*]

[a] *University of Oklahoma, Norman, OK 73019, USA*
[b] *Department of Mechanical Engineering, University of Alabama, Tuscaloosa, AL 35487, USA*

Received 26 June 2007; received in revised form 5 December 2007; accepted 13 December 2007

Abstract

Vortical structures formed in evolving jets are important in applications such as fuel injection in diesel engines and fuel leaks. When the jet fluid is different from the ambient fluid, the buoyancy can play an important role in determining the jet flow structure, and hence, the entrainment and fluid mixing processes. In the present study, a jet of helium injected in air is investigated, with emphasis placed on delineating the buoyancy effects on vector–scalar fields during the starting phase. We utilize a computational model, previously validated to predict the flow field of low-density gas jets. The model incorporates finite volume approach to solve the transport equation of helium mass fraction coupled with conservation equations of mixture mass and momentum. Computations were performed for a laminar jet to characterize the advancing jet front, and to capture the formation and propagation of vortex rings and the related pinch-off process. Results show significant effects of buoyancy on jet advancement, as well as on vorticity and helium concentration in the core of the vortex rings.

Keywords: Transient jets; Buoyancy; Vortex ring; Flow dynamics

1. Introduction

The study of jets has been the subject of immense interest to researchers in the fluid mechanics community, in part, because of their widespread occurrence in nature and engineering systems (Fay, 1973; Gebhart, 1973; Turner, 1973; List, 1982; Rodi, 1982; Klein et al., 2003). The complexity of jet configurations varies from laminar plane jets to buoyant turbulent jets (Rodi, 1982), impinging jets (Chung et al., 2002), and wall jets (Addad et al., 2005), etc. Depending upon the inlet conditions, the jet typically consists of the near-field laminar flow, the far-field turbulent flow, and the transition from the laminar to turbulent flow in between the near and far fields. Both constant density and variable density jets have been investigated in the literature (Klein et al., 2003; Satti and Agrawal, 2006a). In a constant density jet, buoyancy is absent since the jet and ambient fluids are the same. The variable density jets occur because the temperature and/or the concentration of the jet fluid are different from those of the surroundings. In this case, the buoyancy effects can be significant either locally and/or globally. Much of the existing literature is devoted to investigations of steady jets. However, unsteady jets are found in applications such as cloud formation, fuel-oxidizer mixing in diesel engines, pollutant dispersal, and fuel/gas leaks (Lai, 1984). The present study is focused on starting jets produced by the discharge of a low-density jet fluid into an initially quiescent ambient of high density fluid.

A characteristic feature of starting jet is the vortex ring formed by the roll-up of the vortex sheet separating at the edge of the injector. The vortex rings have been the subject of several investigations in the past because they represent a fundamental fluid dynamics phenomenon (Riley, 1998). Didden (1979) created vortex rings by ejecting fluid from a circular nozzle by means of a piston accelerating from rest to a uniform speed. The circulation in the vortex ring increased as the ring propagated downstream, until the piston motion ceased. Direct numerical simulations by

---

[*] Corresponding author. Tel.: +1 205 348 4964; fax: +1 205 348 6419. *E-mail address:* aagrawal@eng.ua.edu (A.K. Agrawal).

[1] Presently with Exa Corporation, Burlington, MA.

0142-727X/$ - see front matter © 2008 Elsevier Inc. All rights reserved.
doi:10.1016/j.ijheatfluidflow.2007.12.002

Nomenclature

d	tube inside diameter (mm)
D_b	mass diffusion coefficient (m^2/s)
f	frequency (Hz)
g	acceleration due to gravity (m/s^2)
r	radial coordinate
Re	jet Reynolds number, $Re = U_j d/\nu_j$
Ri	jet Richardson number, $Ri = gd(\rho_\infty - \rho)/\rho U_j^2$
St	jet Strouhal number, $St = fd/U_j$
U_j	average jet exit velocity (m/s)
v_r	radial component of velocity (m/s)
v_z	axial component of velocity (m/s)
Y	mole fraction
z	axial coordinate

Greek symbols

μ	dynamic viscosity of jet fluid (kg m/s)
ν_j	kinematic viscosity of jet fluid (m^2/s)
ρ_j	density of jet fluid (kg/m^3)
ρ_∞	density of ambient fluid (kg/m^3)

James and Madina (1996) found that the computed values of total circulation and location of the vortex spiral center during the evolutionary phase agreed with the experimental findings of Didden (1979). Reasonable agreement between Didden's experiments (1979) and numerical simulations of vortex ring characteristics was also reported by Heeg and Riley (1997). Gharib et al. (1998) generated vortex rings with different jet exit diameters and piston velocities. They found that the flow field generated with a large piston stroke to diameter (L/D) ratio consists of a leading vortex ring followed by a trailing jet. However, for small L/D ratio, the flow field shows only a single vortex ring. The transition between these two distinct states occurred at L/D of approximately 4, named as the formation number by Gharib et al. (1998). Schram and Riethmuller (2001) used particle image velocimetry to measure the flow field in an impulsively started jet with steady inlet velocity, instead of a finite amount of fluid ejection by a piston in experiments of Didden (1979) and Gharib et al. (1998). Schram and Riethmuller (2001) found that velocity, core diameter, and core circulation of the leading vortex ring increased even after the ring had apparently detached from the shear layer generating it.

In the above studies, the density of the jet fluid was the same as that of the ambient fluid, and hence, the buoyancy was absent. However, release of a fluid into lighter or heavier ambient fluid results in the natural convection phenomena associated with buoyancy in a gravitational field. Turner (1962) classified the resulting flow field as "thermal" or "starting plume". The "thermal" results from a short pulse of buoyancy released, for example, by pushing a column of fluid by piston motion. The "starting plume" forms during the initial phase of steady supply of a buoyant fluid discharged, for example, by a jet into the quiescent ambient. The starting plume could become the "steady plume" after a sufficiently long period of time. Turner (1962) explained that the starting plume consists of a *cap*, which is its advancing front, the boundary layer in the vicinity of the injector exit, and a *corridor* (*or stem*) connecting the two. The stem is the source of energy for the cap and the *vortex rings* are formed within the cap. Turner (1962) modeled the starting plume by combining the solution of a steady plume with that of a thermal. By assuming that the velocity of the thermal is a constant fraction of the steady plume velocity, he obtained a solution describing the flow behavior both in the plume and vortex ring.

The first laminar starting plume experiments were reported by Shlien (1976). From shadowgraph pictures, Shlien (1976) found that the cap convection velocity was independent of height and cap dimensions which indicated geometric similarity in the starting plume. The velocity measurements by Tanny and Shlien (1986) also indicated similarity in the flow field over the limited range of plume heights investigated. In agreement with the assumption of Turner (1962), they found that the cap resembles a thermal with buoyancy fed from its base. Chay and Shlien (1985) used an interferometric technique to obtain detailed temperature measurements at different plume heights. They found that about 37% of the flow injected into the starting plume was convected to the cap. Moreover, the cap convection velocity was affected by the Prandtl number of the injected fluid. Moses et al. (1993) presented an experimental study of the scaling laws for a laminar starting plume. They explained that the cap rises with a constant velocity and grows diffusively in width. However, they did not observe the vortex rings presumably because of the high viscosity fluids used in the experiments.

Finding of a universal formation number in constant density jets prompted Shusser and Gharib (2000) to investigate vortex ring formation in starting buoyant plumes. They proposed a theoretical model based on the Kelvin–Benjamin variational principle to show that the buoyant vortex ring pinches off from the plume when the latter can no longer provide the energy required to sustain a steady vortex ring. The time at the pinch-off (or the formation number) was predicted by assuming that the vortex velocity at pinch-off exceeds the plume velocity. Pottebaum and Gharib (2004) provided experimental evidence of pinch-off in a starting buoyant plume, whereby the vortex ring becomes disconnected from the trailing plume. The pinch-off occurred at formation numbers between 4.4 and 4.9, suggesting the universality of the process for various generation mechanisms.

Recently, Iglesias et al. (2005) performed numerical simulations of starting plumes for different jet-to-ambient temperature ratios. They found that the jet front (or cap) location depended strongly upon the jet-to-ambient temperature ratio and that the circulation in the flow increased at a constant rate. Moreover, the vortex formed in the shear layer entrained a significant amount of jet fluid during the formation and subsequent evolutionary stages. Since the characteristic Froude number was sufficiently large, Iglesias et al. (2005) neglected buoyancy and hence, their solution was dependent only upon the Reynolds number and the jet-to-ambient temperature ratio. However, this assumption is questionable since buoyancy can be significant in localized regions as shown by recent experiments (Yildirim and Agrawal, 2005) and computations (Satti and Agrawal, 2006b) in self-excited low-density gas jets.

Most previous studies have focused on the dynamics of vortex rings for the constant density case. However, much less attention has been given to understand characteristics of starting plume during the evolutionary phase. In particular, none of the past studies have isolated effects of buoyancy on the flow structure of a starting plume. Thus, we consider a low-density gas jet injected into a high-density quiescent atmosphere. The problem is relevant to fuel leaks from high-pressure source (e.g., Houf and Schefer, 2007) or injection of fuel in the oxidizing environment of diesel engines (e.g., Gopalakrishnan and Abraham, 2004). In these applications, the vortex ring in the advancing front promotes molecular mixing between the fuel and oxidizer to form an ignition kernel where combustion can initiate. We employ a comprehensive computational fluid dynamic (CFD) model to simulate the evolving flow structure of the jet in the near-field. The jet and ambient fluids are helium and air, respectively. The flow is considered isothermal and subsonic. Buoyancy effects are isolated by performing computations in earth gravity and zero gravity. In the following sections, we provide details of the computational procedure and then discuss the results.

2. Technical approach

2.1. Governing equations

We have used the CFD model described by Satti and Agrawal (2006a, b) to compute the evolving flow structure of the low-density gas jet. The unsteady, laminar, axisymmetric flow model solves the coupled conservation equations of species mass, and mixture mass and momentum expressed as follows:

$$\frac{\partial\rho}{\partial t}+\frac{\partial}{\partial z}(\rho v_z)+\frac{\partial}{\partial r}(\rho v_r)+\frac{\rho v_r}{r}=0 \tag{1}$$

$$\begin{aligned}\frac{\partial}{\partial t}(\rho v_z)+\frac{1}{r}\frac{\partial}{\partial z}(r\rho v_z v_z)+\frac{1}{r}\frac{\partial}{\partial r}(r\rho v_r v_z)\\ =-\frac{\partial p}{\partial z}+\frac{1}{r}\frac{\partial}{\partial z}\left[r\mu\left(2\frac{\partial v_z}{\partial z}-\frac{2}{3}(\nabla\cdot\bar{v})\right)\right]\\ +\frac{1}{r}\frac{\partial}{\partial r}\left[r\mu\left(\frac{\partial v_z}{\partial r}+\frac{\partial v_r}{\partial z}\right)\right]+(\rho-\rho_\infty)g\end{aligned} \tag{2}$$

$$\begin{aligned}\frac{\partial}{\partial t}(\rho v_r)+\frac{1}{r}\frac{\partial}{\partial z}(r\rho v_z v_r)+\frac{1}{r}\frac{\partial}{\partial r}(r\rho v_r v_r)\\ =-\frac{\partial p}{\partial r}+\frac{1}{r}\frac{\partial}{\partial z}\left[r\mu\left(\frac{\partial v_r}{\partial z}+\frac{\partial v_z}{\partial r}\right)\right]\\ +\frac{1}{r}\frac{\partial}{\partial r}\left[r\mu\left(2\frac{\partial v_r}{\partial r}-\frac{2}{3}(\nabla\cdot\bar{v})\right)\right]-2\mu\frac{v_r}{r^2}+\frac{2}{3}\frac{\mu}{r}(\nabla\cdot\bar{v})\end{aligned} \tag{3}$$

where $(\nabla\cdot\bar{v})=\frac{\partial v_z}{\partial z}+\frac{\partial v_r}{\partial r}+\frac{v_r}{r}$

$$\begin{aligned}\frac{\partial}{\partial t}(\rho Y)+\frac{\partial}{\partial z}(v_z\rho Y)+\frac{\partial}{\partial r}(v_r\rho Y)\\ =\frac{\partial}{\partial z}\left(\rho D_b\frac{\partial Y}{\partial z}\right)+\frac{1}{r}\frac{\partial}{\partial r}\left(r\rho D_b\frac{\partial Y}{\partial r}\right)\end{aligned} \tag{4}$$

Eq. (1) is the continuity equation and Eqs. (2) and (3) are, respectively, the axial and radial momentum conservation equations. Eq. (4) is the species mass conservation equation. The density was computed from the ideal gas law using local pressure and mixture composition (or molecular weight). The dynamic viscosity was computed using Wilke's mixture average formula (Bird et al., 1960) to account for local variations in the mixture composition. The mass diffusivity of helium into air (or air into helium) was taken as a constant.

2.2. Boundary and initial conditions

Fig. 1 shows the computational domain whereby the left-side boundary represents the axis of symmetry. Pure helium was injected from a tube (inside diameter, d) into quiescent air at atmospheric pressure and temperature. The velocity

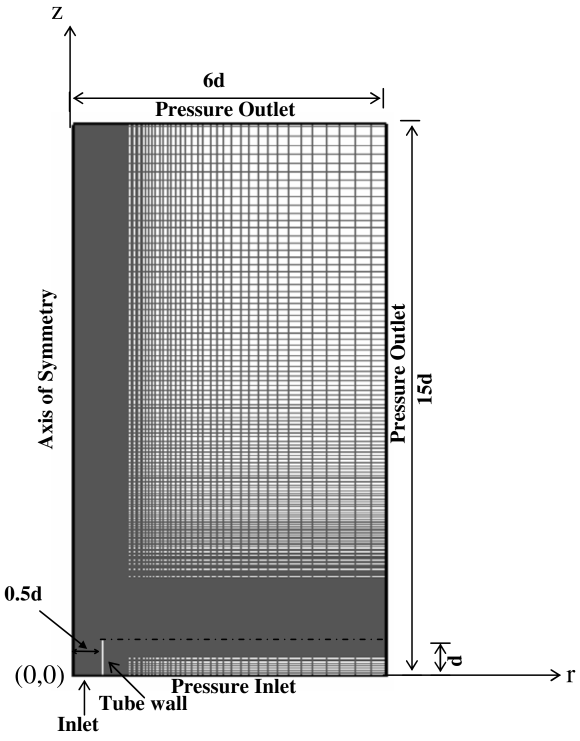

Fig. 1. Schematic of the computational domain.

profile at the tube inlet was fully developed. A finite tube length (1d) was included within the computation domain to accurately replicate diffusion upstream of the tube exit observed in past experimental studies (Cetegen and Kasper, 1996; Pasumarthi and Agrawal, 2003). No slip and zero mass diffusion conditions were imposed on surfaces of the tube wall. The exit and lateral boundaries were specified as pressure outlets, where flow properties are extrapolated from the interior. Pressure inlet condition was imposed at the upstream boundary around the tube. At the start of the calculations, the flow velocities and helium mass fraction were zero throughout the computational domain, except at the tube inlet where the helium mass fraction was unity and the axial velocity profile pertained to fully developed laminar flow. Domain sizes ranging from 10d × 3d (in axial and radial directions) to 50d × 10d were considered initially to evaluate the effect of the domain size on flow predictions. Based on this evaluation, the domain size of 16d × 6d was chosen for further analysis.

2.3. Computational details

An orthogonal grid was generated by splitting the computational domain into five sub regions. The grid points in the radial direction were concentrated to resolve steep gradients in the flow oscillation region (see Fig. 1). The grid spacing was gradually increased in the axial direction. A single grid of one radian was used in the circumferential because of the axisymmetric nature of the problem. The governing equations were discretized using the finite volume approach. The convective terms were discretized using the QUICK scheme and the pressure–velocity coupling was implemented using the SIMPLEC algorithm. The governing equations were solved in a segregated manner using an implicit, second-order time-dependent formulation. To demonstrate grid independence, computational models with different grid sizes were analyzed by Satti and Agrawal (2004). Based on several trials, the grid with 270 axial and 110 radial nodes (270 × 110) and time step of 1.6 ms was found to provide grid independent results in this study. Computations were continued until the flow achieved either periodic oscillations or steady conditions.

2.4. Validation

Satti and Agrawal (2006a,b) validated the numerical model by comparing computations of the unsteady flow

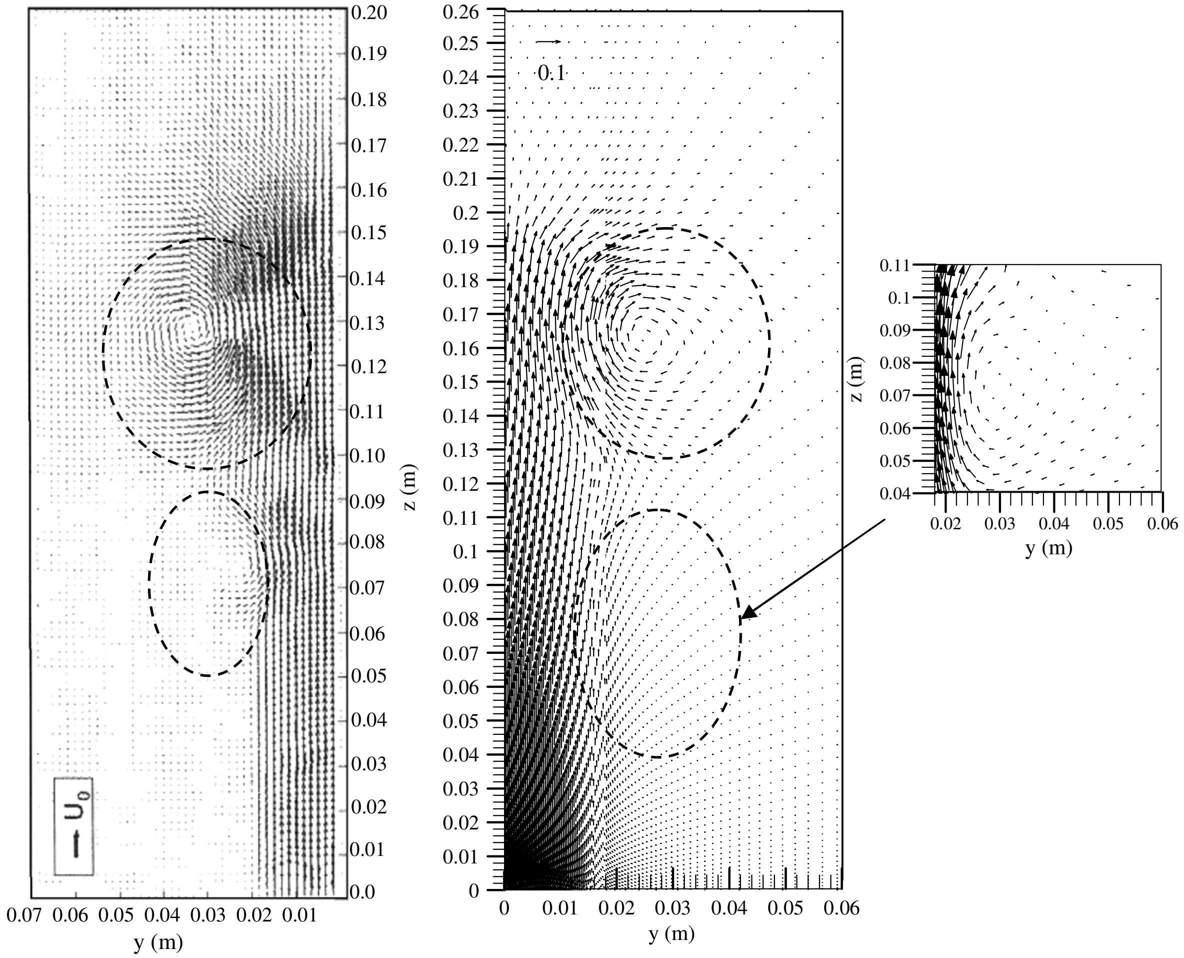

Fig. 2. Comparison of experimental (left) and computational (right) velocity vectors in an evolving air jet in air, $d = 38.0$ mm, $U_j = 0.065$ m/s.

in self-excited helium jets with available experimental results over a range of Richardson number, ($Ri = g.d.(\rho_\infty - \rho_j)/\rho_j U_j^2$) where g is the gravitational acceleration, d is the jet exit diameter, ρ_∞ and ρ_j are the free-stream and jet densities, respectively, and U_j is the mean jet exit velocity). In the present study, the capability of the CFD model to predict the evolving flow structure was validated using existing experimental data for both constant and low density jets. Fig. 2 illustrates a typical velocity field comparison of experimental (Schram and Riethmuller, 2001) and computational results at a particular instant of evolution in a constant density jet. One can identify several common features: (a) the orientation of the velocity vectors in the near injector region indicates a dominant flow in the streamwise direction, (b) the entrainment of the ambient fluid into the vortex ring is illustrated by radial orientation of the flow vectors, and (c) the pinch off at a downstream location results in double vortices in the flow field. Both experimental and computational data reveal an increase in the vortex convection velocity in the

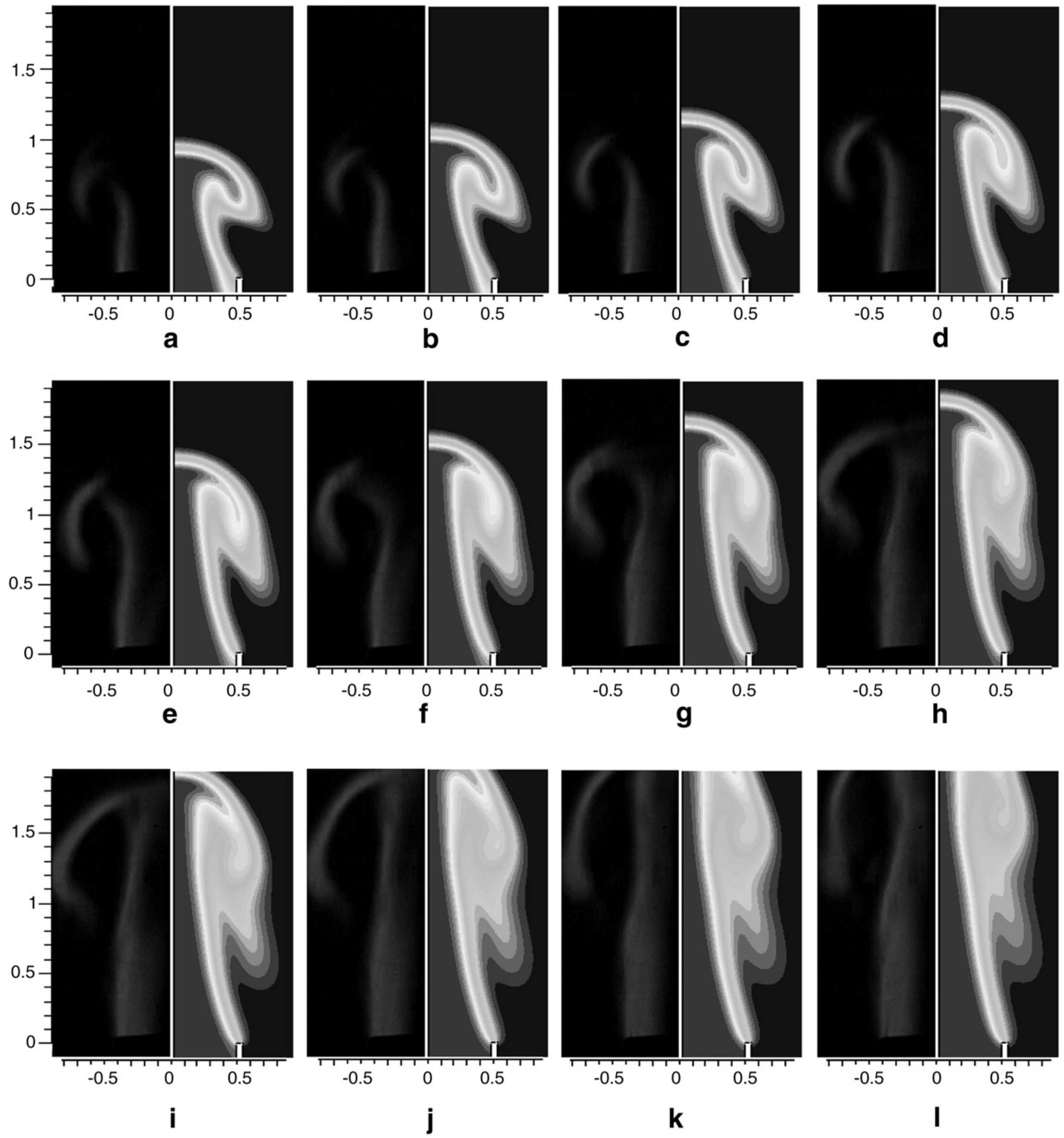

Fig. 3. Comparison of experimental (left) and computational (right) scalar fields in an evolving helium jet in air, $d = 19.05$ mm, $Re = 100$ and $Ri = 3.2$. For experiments, black and white reproductions of color schlieren images are shown. For computations, contour plots of helium mole percentage are shown. The time interval between consecutive images is 0.005 s.

downstream direction. These results illustrate that the present numerical model is capable of capturing the global flow features of an evolving constant density gas jet.

Next, validation results are presented for the variable density jet, i.e., helium injected into quiescent air. Fig. 3 represents a sequence of images depicting the evolving scalar flow structure of an evolving jet in the near field. The operating parameters and time interval of 5 ms between subsequent images are the same for both experiments and computations. The experimental images are the black-and-white reproduction of color schlieren images acquired by the rainbow schlieren deflectometry technique (Pasumarthi and Agrawal, 2003). Thus, the gradations in these images relate to density gradients integrated over the line of sight. In contrast, the computational images show contours of helium mole fraction within the flow field. These differences in image attributes must be taken into consideration when comparing the experimental and computational results. The experimental images in Fig. 3a–f show the jet flow evolving into a mushroom shape structure. Formation of the mushroom shaped structure is also depicted in computations as observed from the related images in Fig. 3. Note that the white region represents the shear layer region both in experimental and computational images. In both experiments and computations, the shape of the mushroom cap, the shroud region, i.e., ends of the mushroom cap, and stem length are remarkably similar. Both experiments and computations show that, at downstream locations, the stem contracts during the formation stage. Farther downstream (Fig. 3g–l), the stem width decreases significantly because of the buoyancy induced acceleration of the jet fluid. Excellent qualitative agreement between computational and experimental results in Fig. 3 yields confidence in the capability of the present model to simulate the unsteady flow structure of evolving low-density gas jets.

3. Results and discussion

Computations were performed for several test conditions, although detailed results are presented only for jet Reynolds number of 300, ($Re = U_j d/\upsilon$, where v is the kinematic viscosity of the jet fluid, $d = 31.8$ mm and $U_j = 1.16$ m/s). The effects of gravity are studied by considering two gravitational levels, $G = 0.0$ and 1.0, where $G = g/9.81$. Understanding of the spatial and temporal development of the jet flow is facilitated by simultaneous visualizations of vector and scalar fields. The computed data are also analyzed to study formation, evolution, and pinch-off processes associated with the vortex ring.

3.1. Cap propagation velocity

We start our discussion with axial movement of the advancing jet front or cap, which is one of the global features of the jet. The cap location was identified as the point on the axis with helium mass fraction of 0.1. Fig. 4a shows the results at different times for $G = 1.0$ and 0.0. For $t < 0.06$ s, the jet front or cap moved to the same axial location both in earth and zero gravity. However, at later times, the cap moved farther downstream in earth gravity, and the difference in the cap location between the two cases increased rapidly with time. For example, at $t = 0.18$ s, the cap in earth gravity was located at $z/d = 5.0$ compared to that at $z/d = 3.0$ in zero gravity. The remarkable difference in the cap location is caused by the buoyant acceleration of the jet fluid in earth gravity as discussed later. The cap convection velocity (normalized by the average jet exit velocity), shown in Fig. 4b, pertains to slope of the curve in Fig. 4a. In earth gravity, the cap velocity decreases until $t < 0.06$ s since the jet momentum must initially overcome the heavier ambient fluid on top. Thereafter, the buoyant acceleration takes over to increase the cap convection velocity from a minimum of 0.75 m/s at $t = 0.06$ s to 1.4 m/s at 0.18 s. Lack of buoyancy in zero gravity decreases the cap velocity at all times. For $G = 0$, the cap velocity decreases rapidly for $t < 0.08$ s and gradually thereafter.

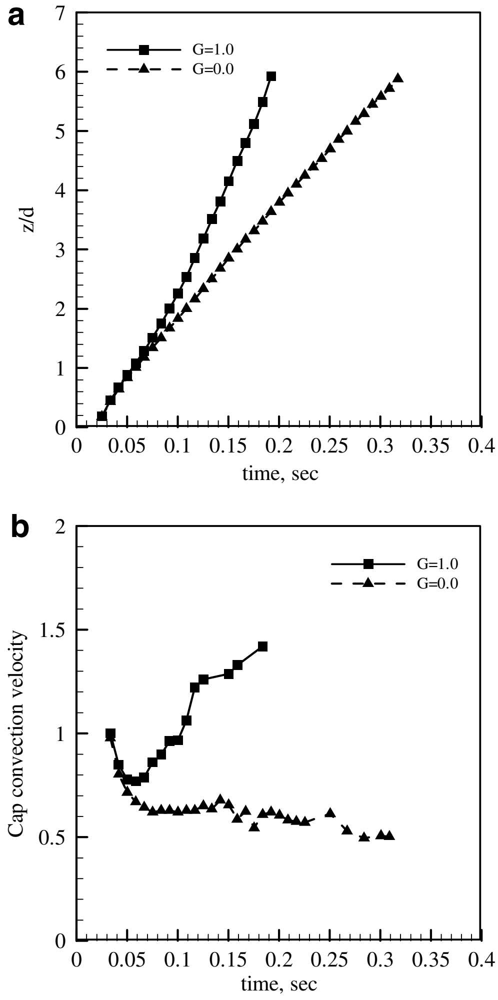

Fig. 4. Plot showing (a) axial location of the cap, and (b) cap convection velocity. $d = 31.8$ mm, $Re = 300$.

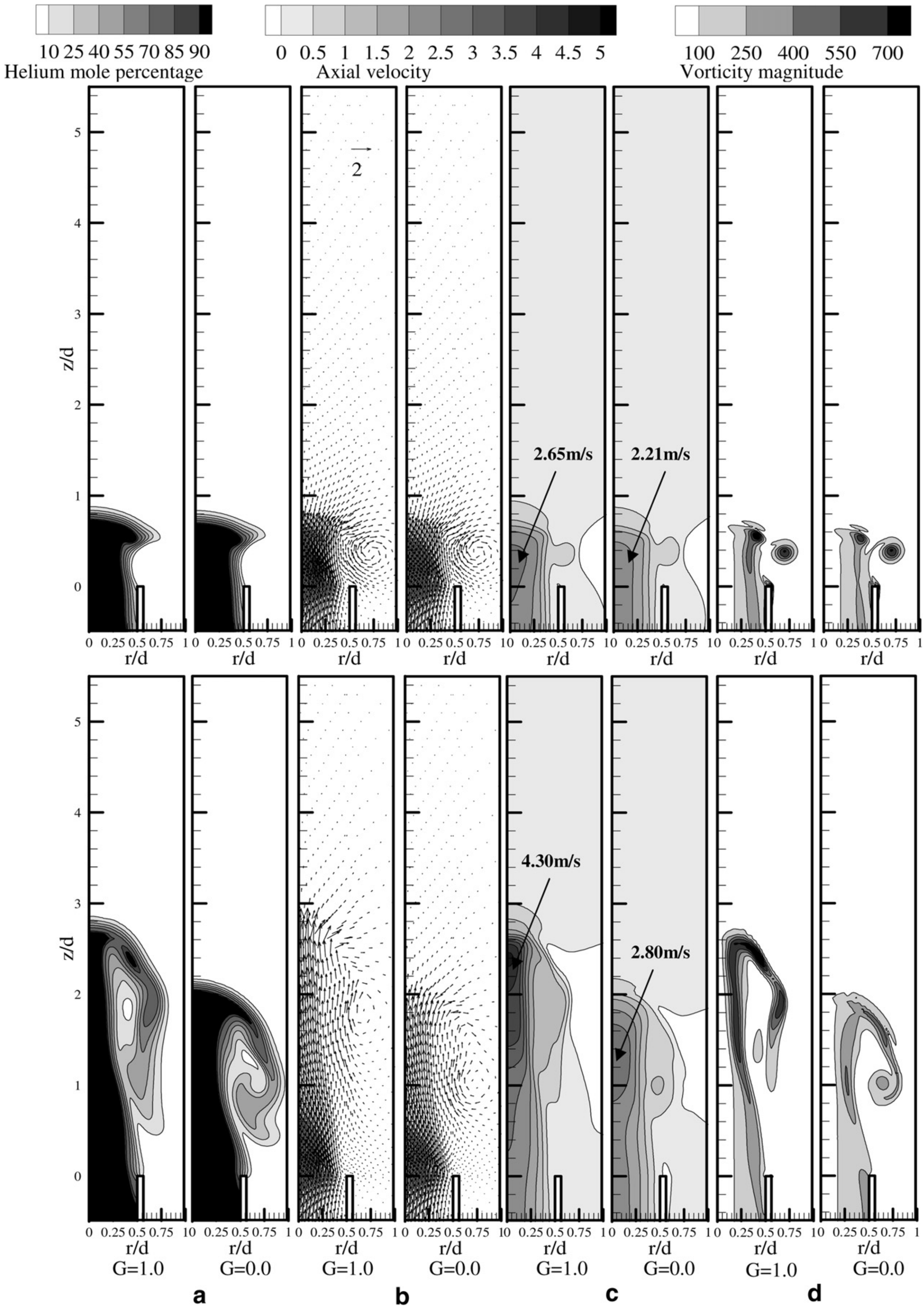

Fig. 5. Contours of: (a) helium mole percentage, (b) velocity vectors, (c) axial velocity, m/s, (d) vorticity magnitude, 1/s for $d = 31.8$ mm, $Re = 300$. $G = 1.0$ (left) and $G = 0.0$ (right). The top row shows results for $t = 0.0501$ s. The bottom row shows results for $t = 0.1169$ s.

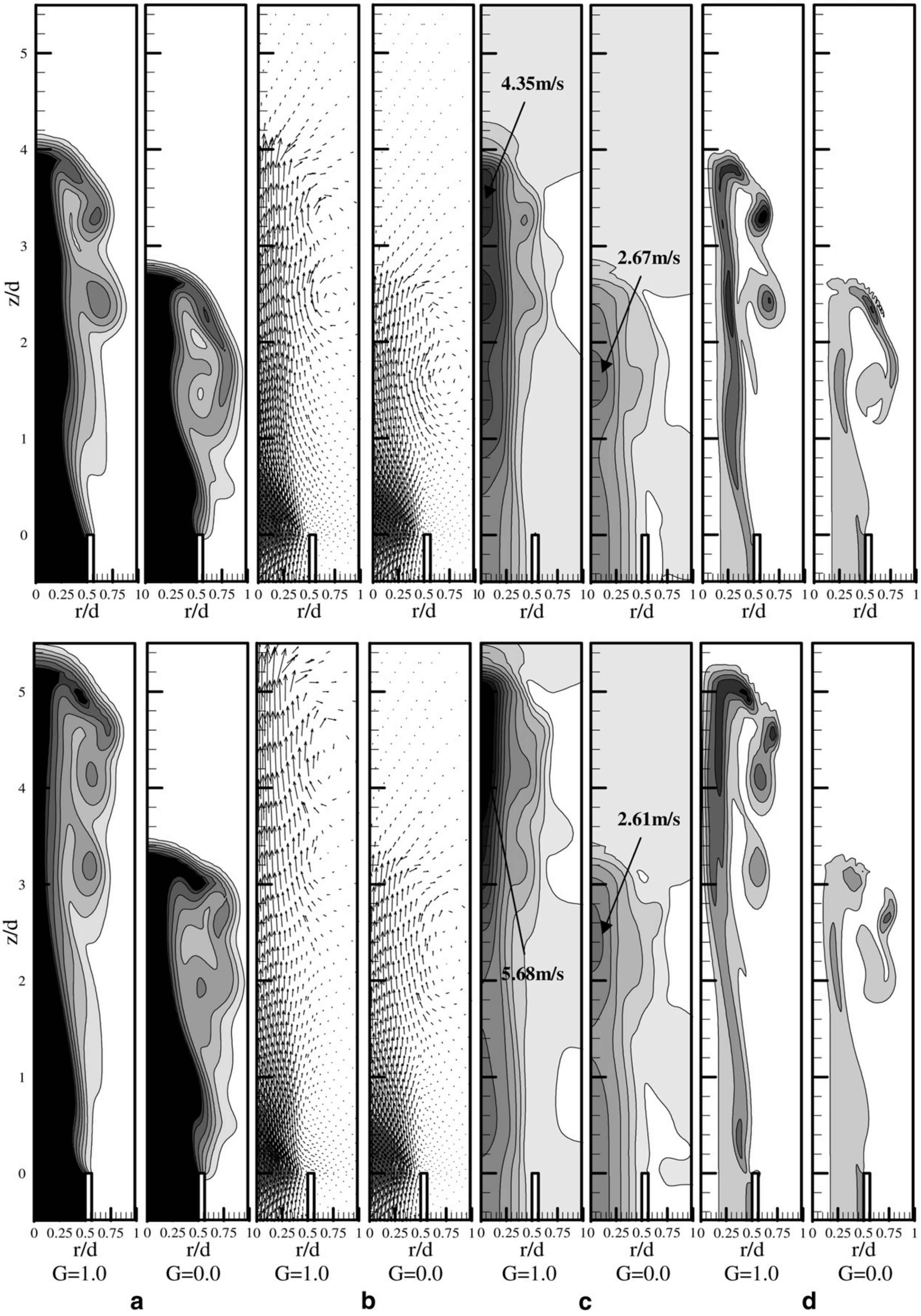

Fig. 6. Contours of: (a) helium mole percentage, (b) velocity vectors, (c) axial velocity, m/s, (d) vorticity magnitude, 1/s for $d = 31.8$ mm, $Re = 300$. $G = 1.0$ (left) and $G = 0.0$ (right). The top row shows results for $t = 0.1503$ s. The bottom row shows results for $t = 0.1837$ s.

3.2. Spatial-temporal development of the evolving jet flow

The flexibility of varying the buoyancy forces in computations was utilized to examine the structural development of the jet at $Re = 300$. Figs. 5 and 6 show contours of helium mole percentage, velocity vectors, axial velocity contours, and vorticity contours for the computed gravity levels of $G = 1.0$ and 0.0 at four instants during the jet evolution. In the beginning stage, i.e., at $t = 0.050$ s, helium mole percentage contours show the typical hemispherical

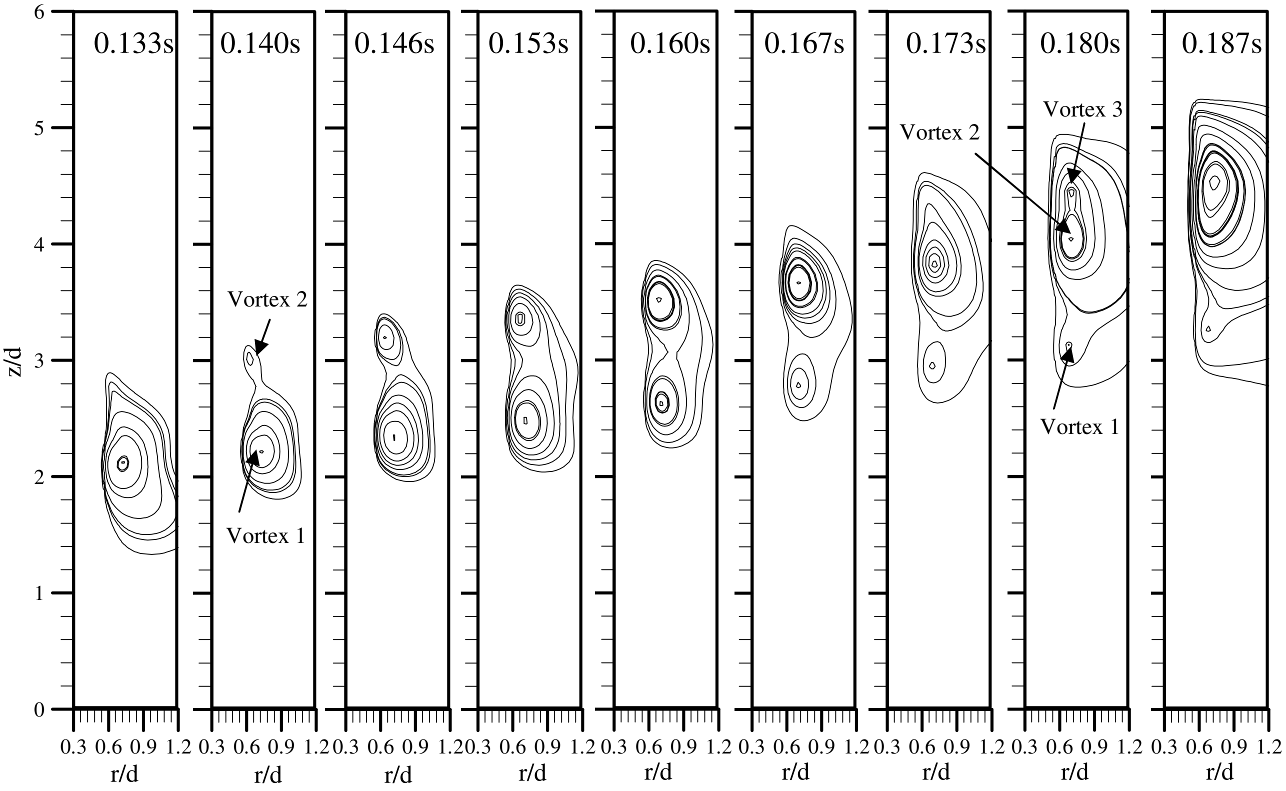

Fig. 7. Stream function contours between $t = 0.133$ s and 0.187 s for $G = 1.0$, $d = 31.8$ mm, $Re = 300$, $Ri = 1.52$.

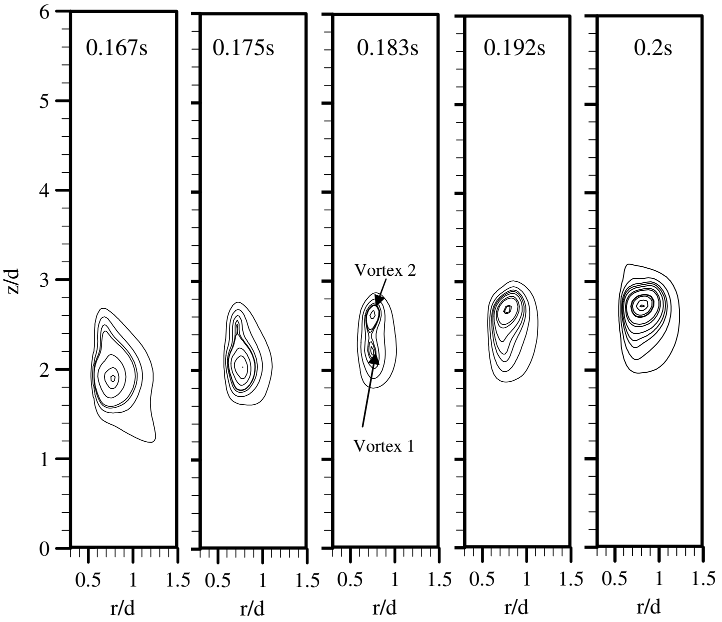

Fig. 8. Stream function contours between $t = 0.167$ s and 0.2 s for $G = 0.0$, $d = 31.8$ mm, $Re = 300$.

dome like structure, both in earth and zero gravity. Although the advancing front or cap broadens, the stem region contracts evidently by entrainment of ambient air into the jet fluid. This explanation is supported by the velocity vectors near the jet exit in Fig. 5b, showing flow recirculation with core situated at $r/d = 0.75$ and $z/d = 0.5$. The vortex ring thus formed appears similar both in earth and zero gravity. For both cases, the axial velocity and vorticity fields also look similar at this instant. The vorticity field clearly depicts recirculation in the vortex ring centered at $r/d = 0.75$ and $z/d = 0.5$. The peak axial velocity at the center of the jet is about 2.6 m/s at $G = 1.0$ compared to 2.3 m/s at $G = 0.0$.

The jet flow structure at $t = 0.117$ s, shown in the bottom part of Fig. 5, reveals mushroom like shape both in earth and zero gravity. However, at this instant, buoyancy has significant influence on the structure of the evolving jet. For example, the cap has advanced to about $z/d = 3.0$ for $G = 1.0$ compared to $z/d = 2.0$ for $G = 0.0$. Helium concentration contours also indicate that the stem is narrower in earth gravity compared to that in zero gravity. The velocity vectors in Fig. 5b show radial entrainment of ambient air into the cap both for $G = 1.0$ and 0.0. However, the size of the velocity vectors in the entrainment region is larger for $G = 1.0$ than that for $G = 0.0$. The vortex core is located at $r/d = 0.74$, $z/d = 1.8$ in earth gravity compared to that at $r/d = 0.75$, $z/d = 1.1$ in zero gravity. In earth gravity, the velocity vectors downstream of the vortex or near the advancing front are larger in size compared to those in the upstream region of the vortex. Evidently, the core region undergoing buoyant acceleration transfers its momentum to the vortex as the jet core interacts with the vortex. In the absence of buoyancy, such transfer of momentum between the jet core and vortex is rather limited. Fig. 5c shows that the peak axial velocity at the jet center has increased to about 4.3 m/s for $G = 1.0$ compared to a value of 2.8 m/s for $G = 0.0$. Vorticity contours show the cap with elongated lobes in earth gravity compared to the cap with shorter lobes in zero gravity. Buoyancy also contributes to vorticity generation within the cap and lobe regions, since the vorticity is higher for $G = 1.0$ compared to that for $G = 0.0$. Results clearly show that the length,

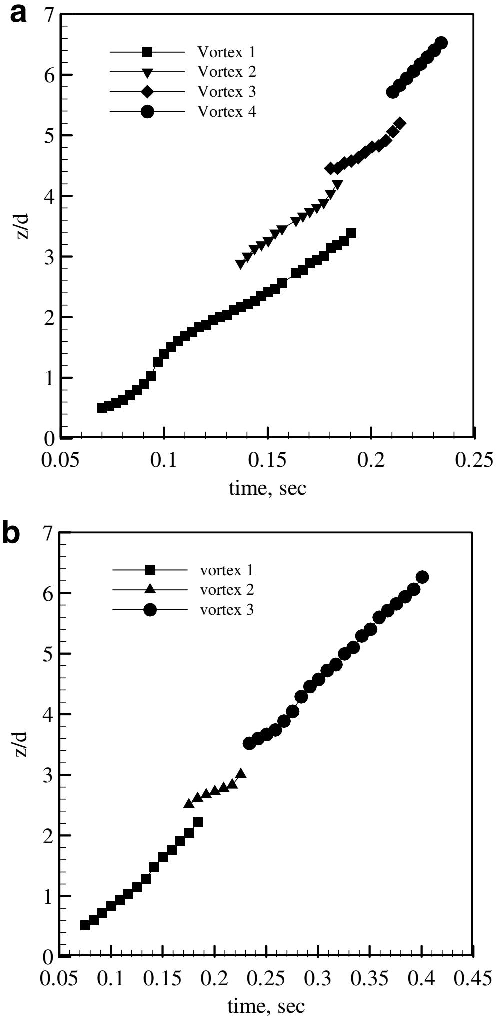

Fig. 9. Axial location of tracked vortical structures, $d = 31.8$ mm, $Re = 300$. (a) $G = 1.0$ and (b) $G = 0.0$.

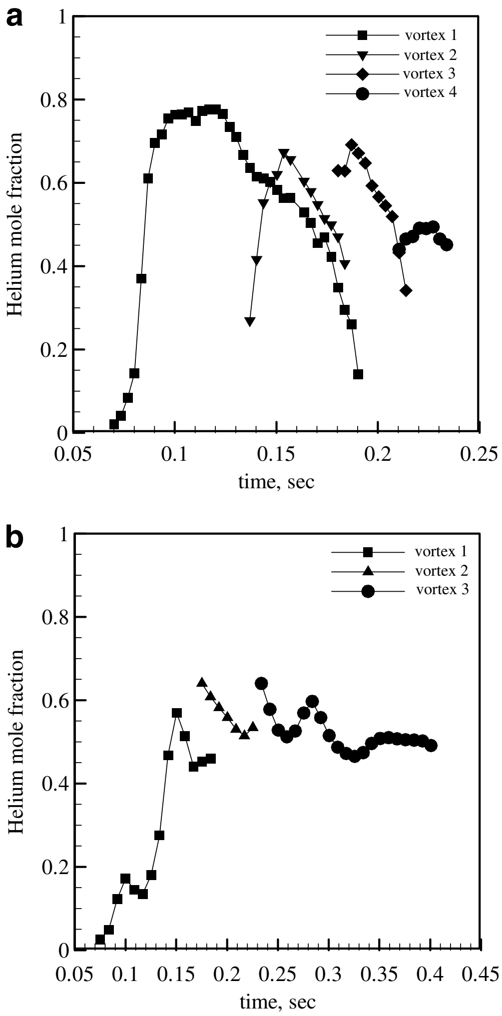

Fig. 10. Helium mole fraction at the core of tracked vortical structures, $d = 31.8$ mm, $Re = 300$. (a) $G = 1.0$ and (b) $G = 0.0$.

width, and shape of the stem, position and shape of the advancing front and lobes around it, entrainment of ambient air, and vorticity generation within the cap and lobes in the evolving jet flow are all influenced by buoyancy.

The jet flow structure at a later time, $t = 0.1503$ s shown in Fig. 6 reveals the interesting phenomena of vortex pinch-off, merging, and dissipation. Helium mole percentage contours, velocity vectors, and vorticity contours all indicate two separate vortex rings at this instant in earth gravity; one centered at $r/d = 0.75$, $z/d = 2.4$ and the other at $r/d = 0.75$, $z/d = 3.3$. The vortex rings pinched-off from the advancing front, and hence, the helium concentration is the highest within the vortex core. Previous studies have shown trailing vortices in constant density jets, and a similar pinch-off phenomenon in starting buoyant plumes was reported by Pottebaum and Gharib (2004). The pinch-off occurs when the circulation level in the vortex ring exceeds a critical value. In zero gravity, only one vortex ring is formed with its core located at $r/d = 0.75$ and $z/d = 1.6$. The peak vorticity in earth gravity is $700\ \text{s}^{-1}$ compared to the peak vorticity of $450\ \text{s}^{-1}$ in zero gravity. Further, the peak axial velocity at $G = 1.0$ is about 4.8 m/s compared to that of 2.7 m/s at $G = 0.0$. The flow structure of the evolving jet at a later time $t = 0.1837$ s reveals features similar to those at $t = 0.1503$ s. Further insight into the vortex dynamics and pinch-odd processes is provided in the following section.

3.3. Vortex dynamics

Figs. 7 and 8 show the stream function contours at different times to illustrate the vortex ring formation and pinch-off processes occurring during the jet evolution. At $G = 1.0$ (Fig. 7), the first plot for $t = 0.133$ s depicts a vortex ring with its core located at $z/d = 2.1$. Later on at $t = 0.140$ s, as the jet convects downstream, one can observe a secondary vortex ring forming at around $z/d = 3.0$. This secondary vortex ring now becomes the leading vortex followed by the trailing vortex core centered at around $z/d = 2.2$. Between $t = 0.146$ s and 0.173 s, the stream function contours show gradual increase in the size and shape of the leading vortex (vortex 2) connected to the advancing front. During the same time, the trailing vortex (vortex 1) gradually dissipates since it is cutoff from the advancing front or the source of energy. Further, at $t = 0.180$ s, a third vortex is formed, which rapidly merges with the leading vortex at $t = 0.187$ s. In the meantime, the trailing vortex dissipates gradually. The stream function plot for $G = 0.0$ in Fig. 8 shows a similar phenomenon of vortex ring formation and pinch off at $t = 0.183$ s. In this case, the pinch-off occurs only once during the evolution stage.

The stream function plots were analyzed to track different vortex rings formed during the evolution stage for both $G = 1.0$ and 0.0. Fig. 9 plots the axial location of the vortex core at different times. For $G = 1.0$, four different vortex rings were found and tracked in Fig. 9a as opposed to only three vortex rings in zero gravity in Fig. 9b. For $G = 1.0$, vortex 1 and 2 co-exist for significant duration ($t = 0.13$–0.19 s), which is not the case for $G = 0.0$. These interesting differences in vortex ring formation once again signify the importance of buoyancy during the jet evolution process.

Next, helium mole fraction and vorticity inside the vortex core were tracked to quantify the buoyancy effects. Fig. 10a plots the helium mole fraction within the vortex cores at different times during the evolution process for $G = 1.0$. Vortex 1 pertains to the early evolution stage, whereby the jet fluid is just ejected into the ambient. During the initial stages of the evolution, at $t = 0.07$ s, the vortex core contains mainly the ambient fluid. As the jet evolves, the advancing front provides energy feedback to the lobe region to increase the helium mole fraction within the vortex core. At $t = 0.12$ s, the core of vortex 1 reaches a peak helium mole fraction of 0.8. Later, at $t = 0.13$ s, the pinch-off process forms vortex 2 with core helium mole fraction of 0.25. Next, the helium mole fraction at the core of vortex 2 increases because of the feedback from the advancing front. However, the helium mole fraction inside

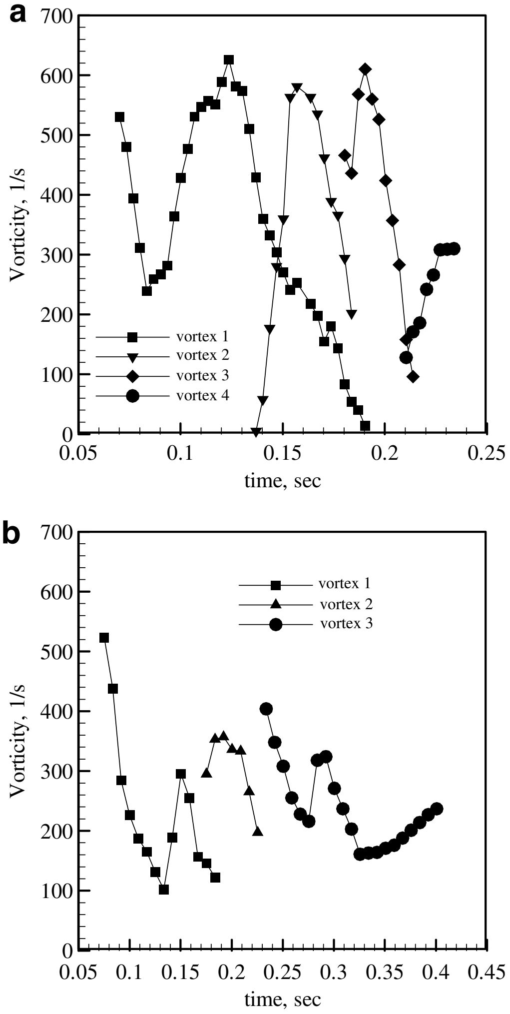

Fig. 11. Vorticity at the core of tracked vortical structures, $d = 31.8$ mm, $Re = 300$. (a) $G = 1.0$ and (b) $G = 0.0$.

vortex 1 decreases since it being separated from the advancing front, dissipates gradually by interacting with the ambient fluid. Similar interactions occur at later times between vortices 2 and 3.

For $G = 0.0$ (Fig. 10b), vortex 1 behaves similar to vortex 1 for $G = 1.0$, i.e., the helium mole fraction within the core increases initially as the vortex interacts with the advancing front, and subsequently, it decreases after the vortex pinches-off from the cap. The peak helium mole fraction in the vortex core in zero gravity is 0.6 compared to that of 0.8 in earth gravity. In zero gravity, vortex 2 forms in a region of high helium concentration, unlike that in the ambient fluid in earth gravity. Fig. 11 plots vorticity magnitude inside the vortex core for $G = 1.0$ and $G = 0.0$. Core vorticity decreases soon after the vortex is formed both in earth gravity and zero gravity. Subsequently, the core vorticity increases as the vortex interacts with the jet and advancing front. This interaction leads to higher peak vorticity in the buoyant jet; peak vorticity for $G = 1.0$ is 600 s^{-1} compared to that of 400 s^{-1} for $G = 0$. After reaching peak vorticity, the vortex dissipates gradually for both $G = 1.0$ and 0.0. Similar features are observed for vortices formed at later stages.

Based on the above discussion, one can clearly appreciate the prominent role played by buoyancy on the global evolution characteristics of a starting jet. In particular, the mechanism of generation and dissipation of vortices is strongly affected by buoyancy. In earth gravity, the buoyant acceleration of the jet fluid rapidly increases the vorticity distribution in the thin mixing at the interface between the two fluids around the stem. This additional vorticity acts as an energy source to sustain circulation within the vortex ring and it also results in pinch-off throughout the evolution phase. However, in zero gravity, a lack of the additional vorticity by buoyant acceleration and dominant diffusion processes result in insufficient circulation in the vortex rings, and hence, in less frequent pinch-off during the evolutionary phase.

3.4. Temporal evolution of velocity and concentration fields

To gain understanding of the jet flow after the initial transients had subsided, computed data at specified axial planes were placed sequentially in time to generate the temporal evolution plots at $z/d = 0.25$ as shown in Fig. 12. The helium mole fraction and axial velocity profiles in Fig. 12 are shown only for $t = 0.0$–0.35 s, although computations were carried out for a much longer duration to completely eliminate the initial transients. Fig. 12 shows that helium arrives at the specified axial location at $t = 0.03$ s. For $t < 0.05$, the jet develops the same way both in earth and zero gravity. Helium mole fraction profiles show that the jet core at $z/d = 0.25$ contracts initially and then, expands at $t > 0.05$ s. In earth gravity, jet expansion is accompanied with large-amplitude fluctuations, which reach a fully oscillatory mode at $t > 0.2$ s. For example, well-defined periodic oscillations in helium concentration occur between $r/d = 0.35$ and 0.6, while pure helium is present at all times for $r/d < 0.3$. The axial velocity field also shows buoyancy-induced periodic oscillations after an initial phase, and the oscillation amplitude is the highest at the jet center ($r/d = 0$). Note that the oscillation amplitude for helium concentration peaks in the jet shear layer unlike the axial velocity with peak fluctuations at the jet center.

Similar to earth gravity, the jet contracts between $t = 0.03$ s and 0.05 s in zero gravity. The jet contraction relates to the entrainment of the ambient air, which forms the initial vortex ring. Subsequently, the jet expands and

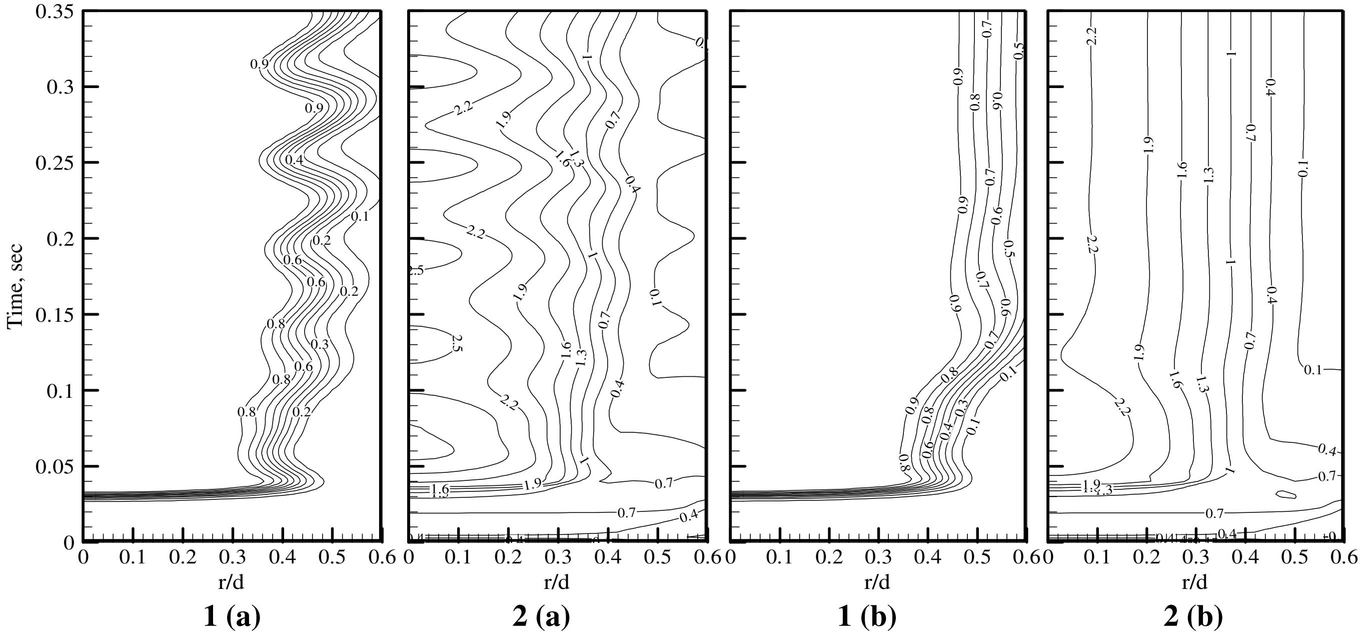

Fig. 12. Temporal evolution of (1) helium mole fraction and (2) axial velocity at $z/d = 0.25$, $d = 31.8$ mm, $Re = 300$. (a) $G = 1.0$ and (b) $G = 0.0$.

after a brief period of waviness in the helium concentration field, steady state is reached at $t \cong 0.25$ s when both helium mole percentage and axial velocity profiles show stratified layers. In summary, after an initial evolutionary phase, the jet exhibits a self-excited oscillatory instability in earth gravity. No instability is observed in zero gravity, since the jet attains a steady flow.

4. Conclusions

The flow structure of an evolving low-density helium gas jet was computed to explain the role of buoyancy on jet front location, and on formation and propagation of the vortex rings. The computational model was successful in capturing the unsteady flow structure details including the mushroom-shaped jet front, multiple vortex rings, and the related pinch-off process. Results show that the jet front initially decelerates, and then, accelerates by buoyancy in earth gravity. In zero-gravity, the jet front does not accelerate, and hence, its axial position always lags behind the axial position of the jet front in earth gravity. In addition, the length, width, and shape of the jet stem, shape of the advancing front and lobes around it, entrainment of ambient fluid into the jet, the pinch-off process, and vorticity generation in the vortex rings are all influenced by buoyancy. Buoyancy also affected vortex ring characteristics; four vortex rings were formed in earth gravity compared to three in zero gravity, peak helium mole fraction in the vortex core in earth gravity was 0.8 compared to that of 0.6 in zero gravity, and peak vortex core vorticity in earth gravity was $600\ \mathrm{s}^{-1}$ compared to $400\ \mathrm{s}^{-1}$ in zero gravity. After a brief evolutionary phase, the jet exhibits self-excited periodic oscillations in earth gravity, while it attains steady, columnar shape in zero gravity.

Acknowledgements

This research was supported in part by grant NNC04-GA22G by NASA's Office of Biological and Physical Research.

References

Addad, Y., Benhamadouche, S., Laurence, D., 2005. The negatively buoyant wall jets: LES results. International Journal of Heat and Fluid Flow 25, 795–808.

Bird, R.B., Stewart, W.E., Lightfoot, E.N., 1960. Transport Phenomena, first ed. Wiley, New York.

Cetegen, B.M., Kasper, K.D., 1996. Experiments on the oscillatory behavior of buoyant plumes of helium and helium–air mixtures. Physics of Fluids 8 (11), 2974–2984.

Chay, A., Shlien, D.J., 1985. Velocity field measurements of a laminar starting plume. Physics of Fluids 29, 2358–2366.

Chung, Y.M., Luo, K.H., Sandham, N.D., 2002. Numerical study of momentum and heat transfer in unsteady impinging jets. International Journal of Heat and Fluid Flow 23, 592–600.

Didden, N., 1979. On the formation of vortex rings: Rolling-up and production of circulation. Journal of Applied Mathematics and Physics 30, 101–116.

Fay, J.A., 1973. Buoyant plumes and wakes. Annual Review of Fluid Mechanics 5, 151–160.

Gebhart, B., 1973. Instability, transition, and turbulence in buoyancy-induced flows. Annual Reviews of Fluid Mechanics 5, 213–246.

Gharib, M., Rambod, E., Shariff, K., 1998. Universal time scale for vortex ring formation. Journal of Fluid Mechanics 360, 121–140.

Gopalakrishnan, V., Abraham, J., 2004. "Computed NO and soot distribution in turbulent transient jets under diesel conditions. Combustion Science and Technology 176, 603–641.

Heeg, R.S., Riley, N., 1997. Simulations of the formation of an axisymmetric vortex ring. Journal of Fluid Mechanics 339, 199–211.

Houf, W., and Schefer, R., 2007. Small-scale unintended releases of hydrogen, Annual Hydrogen Conference and Hydrogen Expo., March 19–22, 2007, San Antonio, TX.

Iglesias, I., Vera, M., Sanchez, A., 2005. Simulations of starting gas jets at low Mach numbers. Physics of Fluids 17, 3.

James, S., Madina, C.K., 1996. Direct numerical simulation of a laminar vortex ring. Physics of Fluids 8, 2400–2414.

Klein, M., Sadiki, A., Janicka, J., 2003. Investigation of the influence of Reynolds number on a plane jet using direct numerical simulations. International Journal of Heat and Fluid Flow 24, 785–794.

Lai, J.C.S., 1984. Unsteady effects in mechanically excited turbulent plane jets. International Journal of Heat and Fluid Flow 5, 215–221.

List, E.J., 1982. Turbulent jets and plumes. Annual Reviews of Fluid Mechanics 14, 189–212.

Moses, E., Zochhi, G., Libchaber, A., 1993. An experimental study of laminar plumes. Journal of Fluid Mechanics 251, 581–601.

Pasumarthi, K.S., Agrawal, A.K., 2003. Schlieren measurements and analysis of concentration field in self-excited helium jets. Physics of Fluids 15 (12), 3683–3692.

Pottebaum, T.S., Gharib, M., 2004. The pinch-off process in a starting buoyant plume. Experiments in Fluids 37, 87–94.

Riley, N., 1998. The fascination of vortex rings. Applied Scientific Research 58, 169–189.

Rodi, W., 1982. Turbulent buoyant jets and plumes. International Journal of Heat and Fluid Flow 3 (4), 194.

Satti, R.P., and Agrawal, A.K., 2004. Numerical Analysis of Flow Evolution in a Helium Jet Injected into Ambient Air. ASME Heat Transfer/Fluids Engineering Summer Conference, Paper No. HT-FED2004-56811, Charlotte, North Carolina.

Satti, R.P., Agrawal, A.K., 2006a. Flow structure in the near field of buoyant low density gas jets. International Journal of Heat and Fluid Flow 27, 336–347.

Satti, R.P., Agrawal, A.K., 2006b. Computational analysis of gravitational effects in low-density gas jets. AIAA Journal 44, 1505–1515.

Schram, C., Riethmuller, M.L., 2001. Vortex ring evolution in an impulsively started jet using digital particle image velocimetry and continuous wavelet analysis. Measurement Science and Technology 12, 1413–1421.

Shlien, D.J., 1976. Some laminar thermal and plume experiments. Physics of Fluids 8, 1089–1098.

Shusser, M., Gharib, M., 2000. A model for vortex ring formation in a starting buoyant plume. Journal of Fluid Mechanics 416, 173–185.

Tanny, J., Shlien, D.J., 1986. Scalar field measurements of a laminar starting plume using digital processing of interferograms. Physics of Fluid 29, 1027–1032.

Turner, J.S., 1962. The Starting Plume in Neutral Surroundings. Journal of Fluid Mechanics 13, 356–368.

Turner, J.S., 1973. Buoyancy effects in fluids. Cambridge University Press.

Yildirim, B.S., Agrawal, A.K., 2005. Full-field measurements of self-excited oscillations in momentum-dominated helium jets. Experiments in Fluids 38, 161–173.